RESEARCH ARTICLE

Editor's Choice

ADVANCED MATERIALS INTERFACES Open Access

www.advmatinterfaces.de

Mimicking Cacti Spines via Hierarchical Self-Assembly for Water Collection and Unidirectional Transport

Melina Weber, Felix Bretschneider, Klaus Kreger, Andreas Greiner, and Hans-Werner Schmidt**

Nature utilizes bottom-up approaches to fabricate defined structures with highly complex, anisotropic and functional features. One prominent example is cacti spines, which exhibit a hierarchically structured conical morphology with a longitudinal microstructured surface. Here, a bottom-up approach to fabricate supramolecular microstructured spines is presented by applying a self-assembly protocol. Taking advantage of the capillary forces of vertically aligned polyamide microfibers acts as the structure-directing substrate for site-specific self-assembly of a specific 1,3,5-benzenetricarboxamides from the solution. The morphology of the supramolecular spines covers several hierarchical levels, ultimately resulting in a conical shape with longitudinal self-assembled microgrooves and a superhydrophilic surface. It is demonstrated that these hierarchical conical microstructures are able to transport water droplets unidirectionally.

1. Introduction

Self-assembly of molecular building blocks by non-covalent interactions results in reversible supramolecular polymers that can form nanostructures with properties beyond those of the individual building blocks.[1–3] Nature uses self-assembly processes across different hierarchical levels to achieve complex meso- and macroscopic morphologies that result in a multitude of highly adapted functionalities.[4] Among the numerous complex morphologies in nature, structures based on the macromolecular building block collagen[5] represent an intriguing example of hierarchy and their associated functionalities for skin, tendons, and bones.[4,6] Another outstanding example is the conical microstructured morphology of cacti spines featuring distinct hierarchical levels.[7–9] Cacti spines can transport water directionally from the spine's tip to the base rendering them the critical component to ensure the water budget of the plant.[7,10,11] To achieve this goal, cacti spines utilize three general structural features as driving forces for the water collecting and transport mechanism.[7] This includes a conical structure which leads to a LAPLACE pressure difference at the water droplet resulting in a unidirectional water transport,[7,12] microgrooves along the spine axis that guide the droplets to the spine base[7] and a roughness gradient from the tip to the base of the spine. The latter two establish a wettability gradient along the spine.[7] Many different approaches have been reported[13–15] to take advantage of these effects and to realize artificial spines by using complex methods such as a combination of electrospinning with a sacrificial template method,[16] an integrative electrochemical corrosion and hydrothermal method,[17] gradient electrochemical corrosion,[18] electrochemical etching,[19] magnetic particle-assisted molding,[20] magnetorheological drawing lithography,[21] a vapor-phase approach[22] 3D-printing[23–25] or a coating technology.[26] However, to the best of our knowledge, a bottom-up approach starting from small molecular building blocks to realize in situ self-assembled hierarchical conical morphologies on the meso and macroscale that mimic cacti spines and their features have not been reported yet.

Here, we present a straightforward method and protocol to fabricate artificial supramolecular microstructured conical spines on top of vertically aligned polyamide (PA) microfibers. The fabrication process of the resulting supramolecular spines can be divided into two steps. The first step involves the electric field-assisted fabrication of vertically aligned PA microfiber arrays, which is also referred to as polymer flock. This process, i.e., electrostatic flocking, is a technique, that is already established on an industrial scale.[27] Hereby, the individual PA microfibers are accelerated in an electrostatic field and vertically oriented onto an adhesive-covered substrate as schematically shown in Figure S1 (Supporting Information). After switching off the electric field, curing the adhesive layer at elevated temperatures and cleaning excess polymer microfibers, a micrograss-like structure is obtained. The unique porous structure of the vertically aligned PA microfibers gives rise to capillary forces in solution-based processes. In a second step, we take advantage of capillary effects in the polymer flock in combination

---

M. Weber, F. Bretschneider, K. Kreger, A. Greiner, H.-W. Schmidt
Macromolecular Chemistry and Bavarian Polymer Institute (BPI)
University of Bayreuth
Universitätsstraße 30, 95447 Bayreuth, Germany
E-mail: greiner@uni-bayreuth.de; Hans-Werner.Schmidt@uni-bayreuth.de

The ORCID identification number(s) for the author(s) of this article can be found under https://doi.org/10.1002/admi.202400101

DOI: 10.1002/admi.202400101

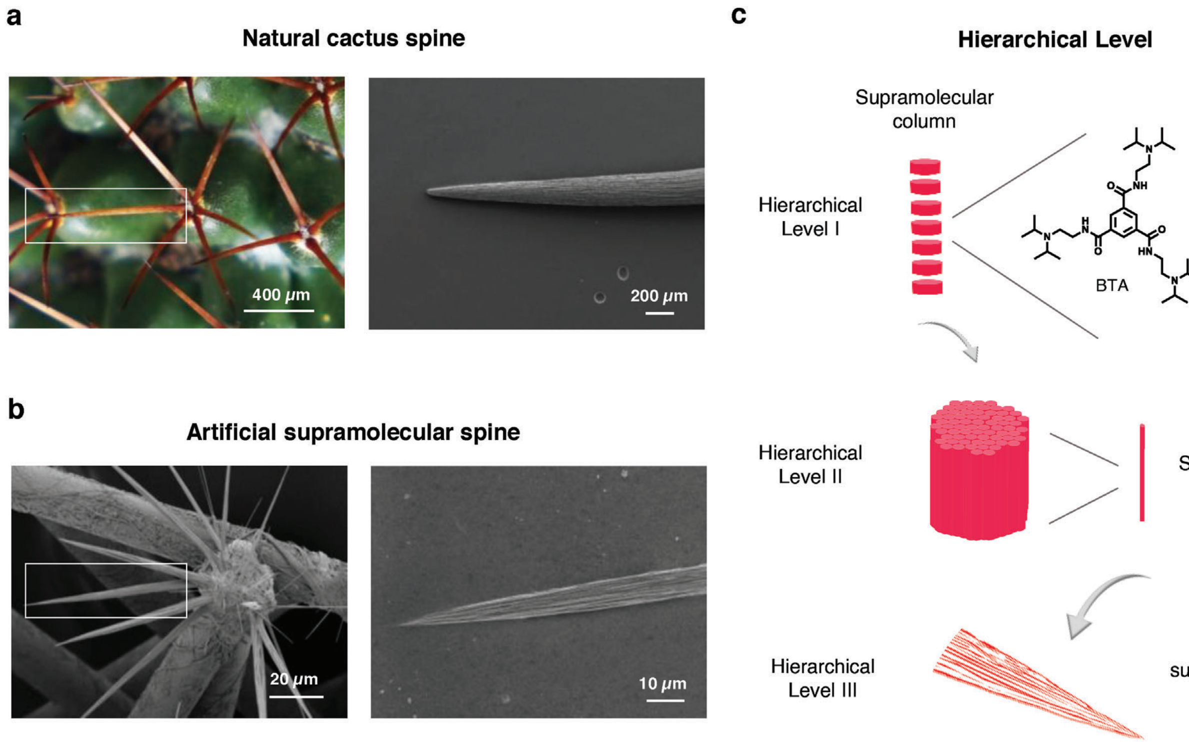

Figure 1. Overview of cacti spines from nature compared to artificial spines of this work and their hierarchical levels. a) Optical image of natural spines from the cactus mammillaria neocoronaria (left) and scanning electron microscopy (SEM) image of a single spine (right). b) SEM images of our artificial supramolecular spines based on BTA building blocks on top of a flocked polyamide microfiber (left) and a single supramolecular spine (right). c) Chemical structure of the 1,3,5-benzenetricarboxamide (BTA) with peripheral *N*,*N*-diisopropylaminoethyl substituents used as molecular building blocks to create artificial spines. Schematic illustration of the self-assembly process covering different hierarchical levels: self-assembly of the molecular building blocks into supramolecular columns (I) further self-assembly of supramolecular columns into supramolecular fibrils (II) and formation of fibrils resulting in the artificial supramolecular spine (III).

with solvent evaporation to initiate directed self-assembly of a dissolved 1,3,5-benzenetricarboxamide (BTA) derivative into ordered supramolecular fibrillar structures. In this class of BTAs, supramolecular structure formation is mainly driven by the formation of three directed helical strands of hydrogen bonds between neighboring molecules.[28] This self-assembly process results in defined supramolecular nano and microfiber morphologies. Such a process is also suitable for larger-scale processing.[29] To obtain the artificial conical microstructures that mimic the hierarchical morphology and function of natural cactus spines (**Figure 1**a) we combine the self-assembly capability of a specific BTA from solution with the PA microfibers. We observed that upon solvent evaporation from 2-propanol and suitable concentrations, self-assembly of the building blocks is predominantly initiated on top of the PA microfibers forming the supramolecular spines (Figure 1b). As a building block, we selected a polar but water-insoluble BTA, namely N^1,N^3,N^5-tris[2 (diisopropylamino)-ethyl]−1,3,5-benzenetricarboxamide to realize the unique morphology of artificial supramolecular spines. This BTA was chosen based on several design principles including i) the ability to self-assemble into fibrillar structures through the formation of three helical strands from hydrogen bonds, ii) insolubility in water to ensure the integrity of the supramolecular structures with respect to water transport applications, and iii) a polar nature of the periphery to realize a hydrophilic surface. Here, the hierarchical levels toward the artificial spine with dedicated function cover three stages as schematically shown in Figure 1c. The dissolved BTA building blocks self-assemble into supramolecular columns (I) by the formation of triple hydrogen bonds. These single columns further self-assemble into defined supramolecular fibrils (II). Ultimately, the supramolecular fibrils form into artificial supramolecular spines (III) with a conical shape and microstructured surface. This is achieved by applying a sophisticated self-assembly protocol within the PA flock. First, the PA flock is partially filled with a BTA solution of 0.50 wt% in 2-propanol. The capillary effects of the dense vertically arranged microfibers lead to the transportation of the BTA solution toward the top of the microfibers. During this process, the solvent evaporates, resulting in highly ordered conical spines which are predominantly formed in situ on top of the PA microfibers. The hierarchical organization of the BTA fibrils as well as the conical shape mimics the hierarchical organization of cacti spines consisting of so-called pillar spines.[9] Typically, natural spines are also constructed from longitudinal fiber strands that build straight fiber bundles as is found in our supramolecular spines.

2. Preparation of Artificial Supramolecular Spines

For the preparation of the artificial supramolecular spines with a conical shape, we found that vertically aligned PA microfibers are

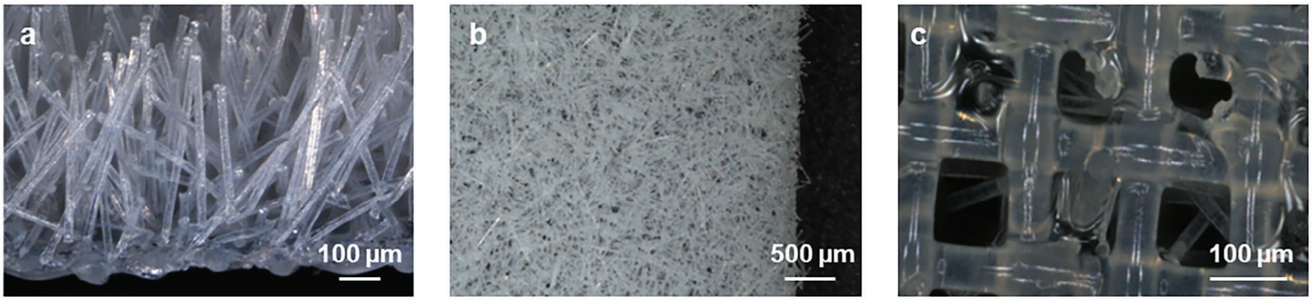

Figure 2. Optical microscope images of the PA flock. a) PA flock side view, b) top view and c) view of the PET mesh from the bottom.

crucial as they provide significant stiffness and polarity to act as structure-directing substrate due to their capillary forces resulting from the microfiber array. Optical microscope images of the PA flock (microfibers with $l = 500$ µm, $d = 19$ µm, $l/d \approx 26$) are depicted in **Figure** 2.

In general, BTAs form supramolecular fibers with a distinct morphology in solution depending on the set of conditions such as selected solvent, concentration, cooling and evaporation conditions. For the specific BTA used in this work, at a constant concentration of 0.50 wt% in 2-propanol a stable solution is present at room temperature and no supramolecular fibers are formed.[30] However, upon evaporation of the solvent, the concentration increases, initiating the self-assembly process and forming evenly round supramolecular BTA fibers with diameters ranging from 150 to 400 nm as shown in Figure S2 (Supporting Information). This situation changes when a concentration of the BTA in 2-propanol is used and evaporation occurs within the PA flock as schematically illustrated in **Figure 3**. While the formation mechanism includes several steps, the directed self-assembly can be described as a simple dip-coating process with subsequent drying that is completed within a few minutes. In detail, the PA flock (Figure 3a) is immersed into a BTA solution and subsequently placed on filter paper to partially remove the BTA solution (Figure 3b). Subsequently, the capillary forces of the vertically aligned PA microfibers transport the BTA solution toward the top of the PA microfiber (Figure 3c). Upon evaporation of the solvent, the local concentration of the BTAs increases at the top of the PA microfibers. Hereby, nuclei are formed that initiate a site-specific self-assembly and supramolecular fiber growth. As evaporation proceeds, additional BTA building blocks are fed to the initially formed BTA fibrils. This process continues until most of the BTA solution in the PA flock is consumed resulting in the formation of hierarchical fibrils that eventually form the conical tips. In this way, supramolecular spines are formed on the top of an individual PA microfiber (Figure 3d).

Close to the end of the evaporation process, evenly round BTA fibers entwined along the PA microfiber and at the bottom of the substrate are formed. The full process is completed within a couple of minutes. The site-specific evaporation-induced self-assembly is supported by observing the drying process by optical microscopy. We have investigated concentrations ranging from 0.05 to 1.0 wt%. Solutions above 0.50 wt% tend to self-assemble at room temperature, rendering them unsuitable for the described process. At the lowest concentration of 0.05 wt%, BTA fibers are only observed along the PA microfibers. Increasing the concentration to 0.10 wt% results in the formation of small fiber-like structures on top of the PA fibers after solvent evaporation. At 0.25 wt%, only small spines form on the PA fibers. However, at a concentration of 0.50 wt%, we observed optimal spine formation on top of the PA fibers. As a result of these findings, we used concentrations of 0.50 wt% for the experiments as optimal processing conditions to consistently produce well-defined supramolecular spines (schematically illustrated in Figure 3d). An optimal set of self-assembly conditions for this specific BTA has been identified. Here, a concentration of 0.50 wt% in 2-propanol with the elaborated drying procedure results in the reproducible formation into conical supramolecular spines. An overview of the PA flock decorated with supramolecular spines and a single PA microfiber with supramolecular BTA spines is depicted in **Figure** 4a. The number of formed supramolecular spines per PA microfiber typically varies from ≈20 (Figure 1b) to 80 and occasionally exceeds 100 spines, which is exemplified in Figure 4. This distribution in the number of spines found on the PA microfibers is a result of the random orientation and local density of the PA microfibers relative to each other giving rise to some local changes in the capillary forces.

3. Supramolecular Spine Morphology

The morphology of the supramolecular spine comprises several hierarchical levels spanning from the nano- to the microscopic scale. The first hierarchical level is the self-assembly of the BTA molecules driven by three strands of hydrogen bonds into single supramolecular columns. The supramolecular columns are densely packed into supramolecular fibrils. These fibrils organize themselves with a high degree of order in the supramolecular spine with a conical shape. The typical morphology of a supramolecular spine can be divided into the tip, middle part and base as depicted in the SEM images in **Figure** 5a. The upper end of the spines tip features a smooth and defined shape with less than 400 nm in diameter (Figure $5a_1$) as a result of the depletion of the molecular building blocks during the in-situ self-assembly process. This indicates the tip is composed of finely structured fibrils. The middle part of the spine features fibril diameters between 500 and 1 µm. The fibrils are aligned in an orientated and dense way forming longitudinal microgrooves (Figure $5a_2$). At the base, the BTA fibrils are more randomly oriented creating a pronounced micro-grooved surface, because of the larger

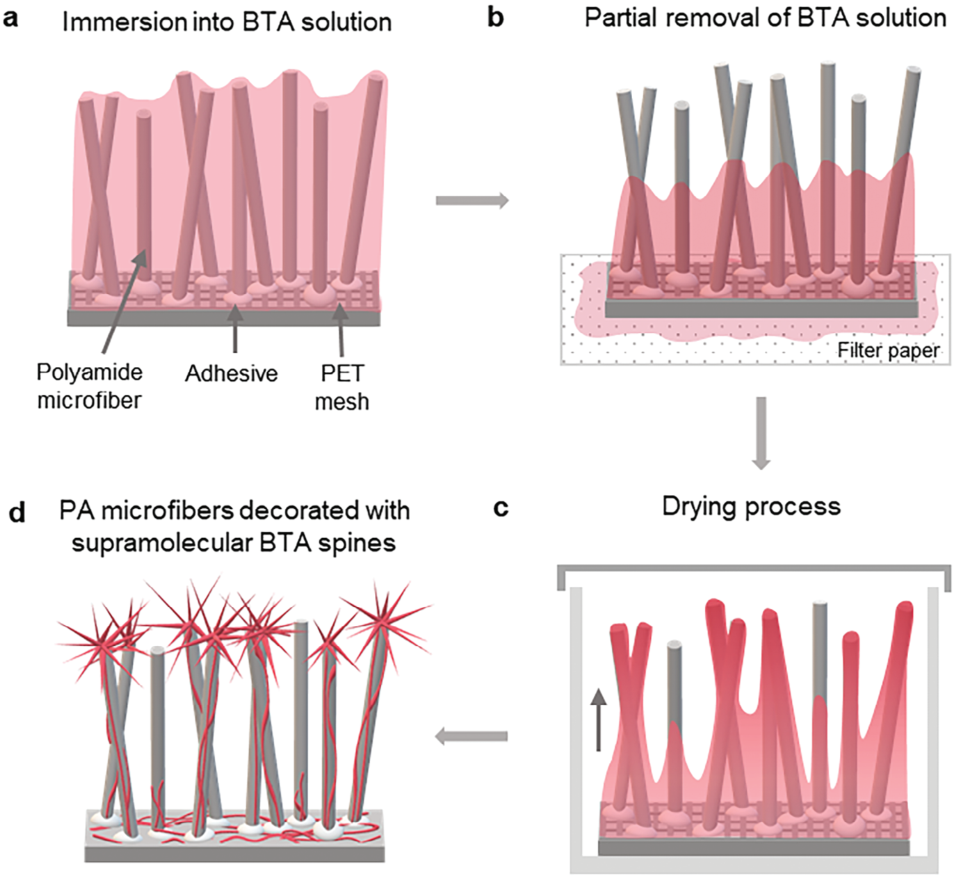

Figure 3. Schematic illustration of the preparation of artificial supramolecular spines on top of polyamide microfibers. a) Polyamide (PA) flock consisting of vertically aligned polyamide microfibers fixed onto a polyethylene terephthalate (PET) mesh. The PA flock is immersed into a BTA solution. b) The soaked PA flock is then placed on a filter paper for a dedicated time to partially remove the BTA solution. c) During the drying process in a covered petri dish capillary forces of the PA microfibers transport the BTA solution toward the PA head and evaporation of the solvent occurs and self-assembly is initiated at the PA head. d) PA microfibers decorated with supramolecular BTA spines.

diameter of the supramolecular fibrils (Figure 5a_3). As a result of these features, which are attributed to the self-assembly process, the supramolecular fibrils become significantly smaller in diameter from the base to the tip of the spine, resulting in a roughness gradient along the spine. Such a roughness gradient along the spine is also depicted in Figure S3 (Supporting Information) showing a high-resolution SEM micrograph of another supramolecular spine with the longitudinal microgrooves. At the base, the average fibrils exhibit diameters up to 1 µm. The transition between the highly orientated supramolecular spines and the PA microfiber head is additionally shown in Figure S4 (Supporting Information). Here, the fibrils are randomly orientated and wrapped around the PA microfiber head and then spread into several high-orientated supramolecular spines. In summary, the supramolecular fibrils are aligned and densely packed with a high degree of order at the tip whereas at the base of the artificial spine, the arrangement of the supramolecular fibrils deviates from the main orientation axis resulting in an overall roughness gradient along the spine. The supramolecular spines exhibit an average length of ≈50 µm and a half apex angle of 6 deg. Further evidence for the high order within the alignment of BTA molecules into the columnar arrangement and thus the orientation of the fibrils along the spines is provided by confocal polarized RAMAN measurements (Figure S5, Supporting Information). Here, the benzene rings of the BTAs show a strong correlation to the angle of the polarizer. When the BTA molecules self-assemble into a columnar arrangement, the benzene rings are stacked on top of each other. Measuring with a parallel polarizer angle along the columns causes a reduced signal of the benzene units, whereas a measurement with a perpendicular polarizer angle relative to the main axis of the spine increases signal intensity. This result provides evidence that single supramolecular columns feature the same orientation as the fibrils and thus the spine.

4. Water Interaction and Transport

The unidirectional water transport from tip to the base found for cacti spines in nature is mainly attributed to three factors, i.e., a LAPLACE pressure difference, longitudinal microgrooves as well as a roughness gradient.[7,12,31] Combining these structural features in artificial spines enables directional water transport.[32] Our supramolecular spines show all of these features, including longitudinal microgrooves due to the alignment of the

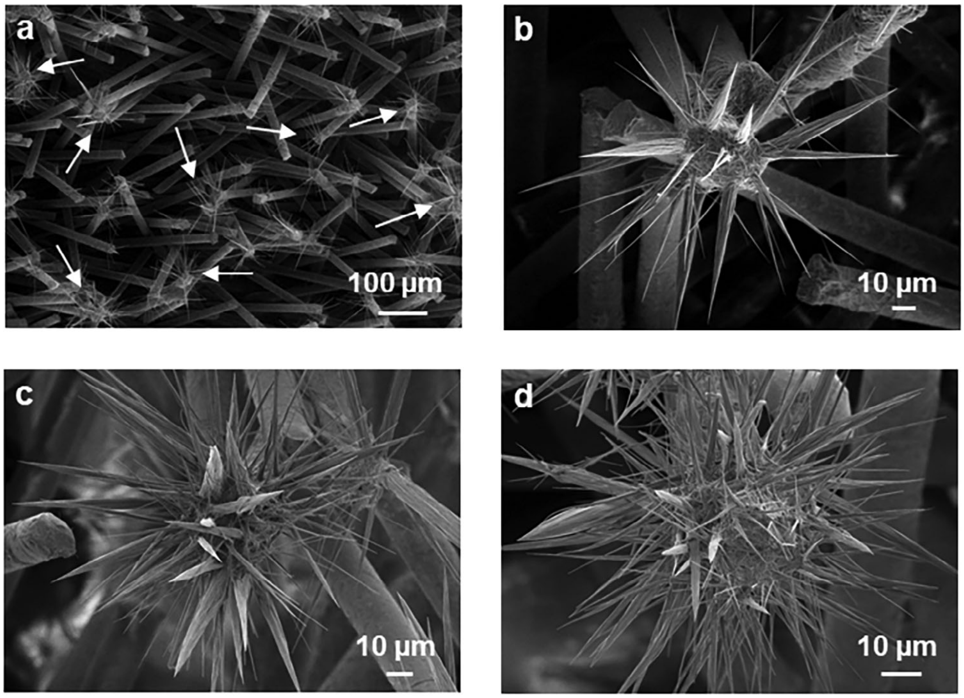

Figure 4. SEM images of the artificial supramolecular spines at the top of PA microfibers. a) SEM of the supramolecular BTA spines at the top of the PA microfibers as overview. b) Single PA microfiber decorated with 33 spines, c) with 81 spines and d) 103 spines, respectively.

supramolecular fibrils and a conical shape as well as a roughness difference increasing from the tip to the base resulting from the varying diameter of the supramolecular fibrils. A roughness gradient across the spine might give rise to a wettability gradient.[33] In this context, we have investigated the wettability of the supramolecular spines with water on isolated single supramolecular spines by environmental scanning electron microscopy (ESEM) at a constant water vapor pressure of 720°Pa (see Figure 5b; Figure S6 and Movie S1, Supporting Information). The middle row of Figure $5b_1$–b_3 depicts the dew collection on the supramolecular spine simulated in the ESEM chamber upon cooling. During the ESEM measurements the stage and subsequently the spines are cooled from 3.9 to 1.9 °C at a cooling rate of 1 °C min^{-1} reaching the dew point at 2.0 °C under these conditions (for details see pressure-temperature phase diagram of water for environmental scanning electron microscopy and dew condensation Figure S6, Supporting Information). The initial state prior to water condensation of the supramolecular spines is shown in Figure $5b_1$. Upon cooling reaching the dew point at ≈2.0 °C, water nucleation occurs, resulting in a complete wetting and filling of the grooves with a larger accumulation of water at the base (Figure $5b_2$). This pronounced spreading of the water across the supramolecular spine suggests a superhydrophilic surface.[34] Upon further cooling to 1.9 °C, water condensation proceeds. Simultaneously, directional water transport from the tip toward the base of the spine takes place as indicated by the formation of a droplet reservoir at the base (Figure $5b_3$). In comparison, ESEM measurements of PA microfibers under the same conditions result only in droplet formation on the microfibers (Figure S7, Supporting Information) revealing a more hydrophobic surface compared to the supramolecular spine. To demonstrate the unidirectional water transport of droplets and the corresponding transport velocity, the supramolecular spines are irrigated with fog. The right row of Figure 5 shows the unidirectional water droplet transport of the captured fog on a supramolecular spine caused by the conical structure, the microgrooves and the roughness gradient. These structural features result in physical phenomena of the water droplet transport at the supramolecular spine (detailed description in Text S8, Supporting Information). Here, the water droplet transport of several supramolecular spines on top of a PA microfiber was monitored by optical microscopy. At first, droplets were collected by the supramolecular spines tip and quickly transported toward the base as shown in Figure $5c_1$–c_3 and the Movie S2 (Supporting Information). The transport velocity of this initial droplet transport was estimated to be ≈150 µm s^{-1}. This value is an average speed determined based on all acquired data from different artificial spines. Compared to the well-investigated model cactus O. microdasys (≈12 µm s^{-1})[7,35,36] the water droplet transportation of our supramolecular spines is significantly faster. We note that during performing the experiments under these conditions we did not observe any change in morphology or failure of the water transport. Also, in agreement with the ESEM findings, it was observed that the supramolecular spine is wetted by the initial droplet transport due to its hydrophilicity and thus we assume the microgrooves to be homogeneously wetted due to the hydrophilic nature and mainly filled with water.[31] However, we cannot exclude the existence of a Cassie–Baxter or a mixed state.[37–42] Despite that, we observe the formation of a water film during fog irrigation due to the spreading of the water droplets. The spreading of the water droplet results in a higher LAPLACE pressure difference. An increase of R_1 and R_2 at the opposite sides of the

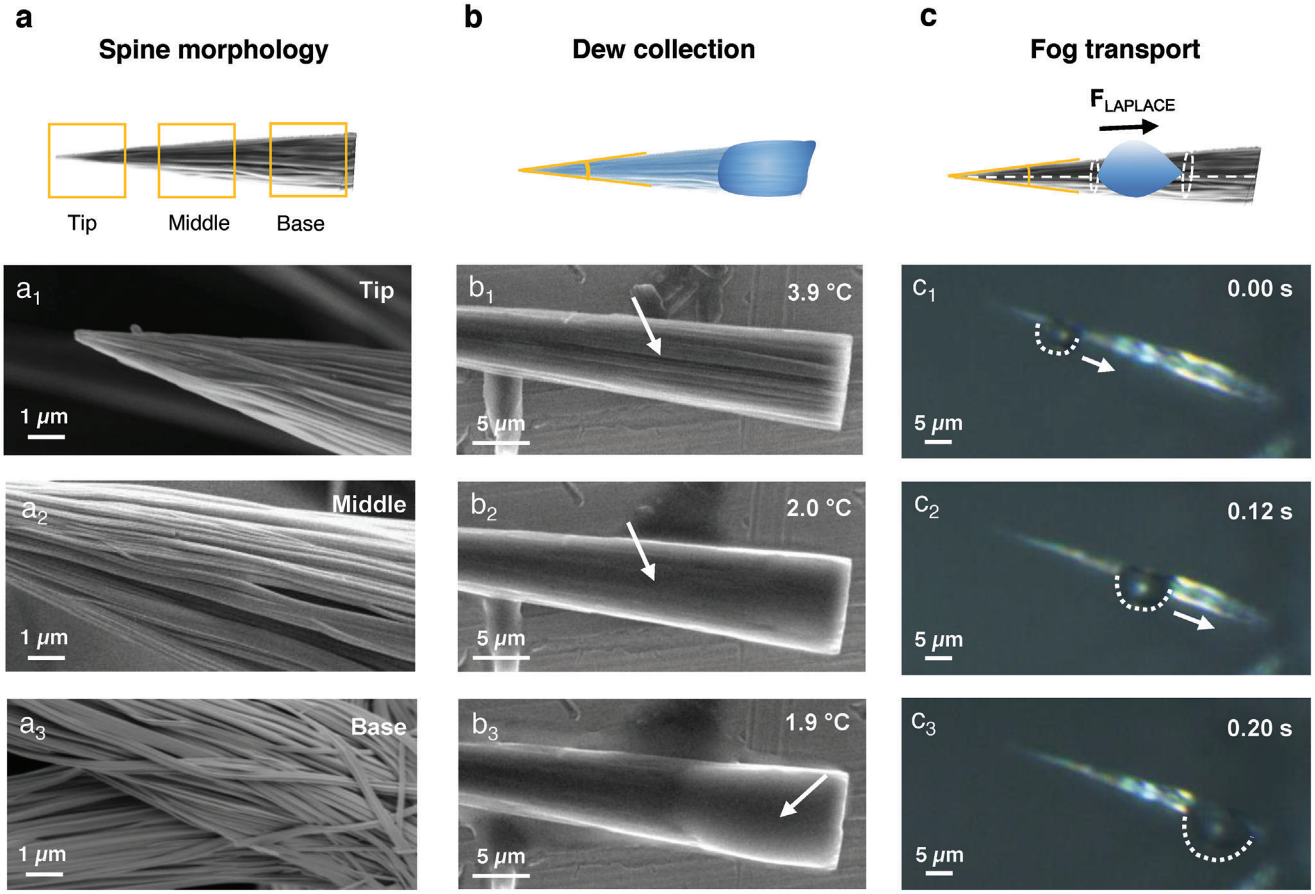

Figure 5. Spine morphology and demonstration of dew collection and fog transport.a) SEM images of the supramolecular spine at different positions (a_1 tip, a_2 middle part, a_3 base). The morphology of the spine shows microgrooves resulting from the hierarchically structured supramolecular fibrils. b) Dew collection on a supramolecular BTA spine observed with an environmental scanning electron microscope (ESEM) at constant water vapor pressure of 720 Pa and different temperatures between 3.9 and 1.9 °C (b_1-b_3). Upon cooling at ≈2.0 °C the dew point is reached and water condensation occurs resulting in a complete wetting and filling of the grooves (b_2). Further cooling to 1.9 °C leads to a water transport toward the base of the spine (b_3). c) Fog transport toward the base of the spine caused by the LAPLACE pressure difference observed with an optical microscope at different times (c_1-c_3). The micrographs show the unidirectional transport of a water droplet.

droplet leads to an overall increased pressure difference resulting in a larger driving force. We postulate that the water film gives rise to an increased water transport. This is schematically shown in Figure S8 (Supporting Information) and has been previously observed in literature—also called the "lubrication effect".[26]

5. Conclusion

We demonstrated a facile and straightforward fabrication of artificial biomimetic supramolecular spines with a conical and hierarchical morphology prepared via a robust site-specific self-assembly process using a specific 1,3,5-benzenetricarboxamides and PA microfiber flock as structure-directing substrate. The supramolecular spines morphology features a conical structure, defined longitudinal microgrooves as well as a roughness gradient mimicking the structural features of natural spines. As a result of the superhydrophilic nature of the conical microstructured surface, these spines are able to efficiently nucleate, collect and transport water droplets. We believe that these biomimetic structures could be highly relevant for water collection applications as shown here. Furthermore, we are convinced that these structures could be suitable for other applications such as transport of liquids, separation and filtration. Additionally, the advantage of the capillary effect of the polymer flock opens the way toward novel structure-directing applications for liquids.

6. Experimental Section

All chemicals were used as received unless otherwise noted. 2-Propanol (100%, VWR), Milli-Q H_2O (18.2 mΩ, < 2 ppb), and *N*,*N*-diisopropylethylenediamine (ABCR) were used. Ethanol and acetone were distilled prior to use. PA microfibers (3.3 dtex/0.5 mm, reinweiß) and a two-component polyester-based flocking adhesive (tubicoll 1510A, L5515) were purchased by Borchert+Moller. Electrostatic flocking was performed with a semiautomatic flocking device (RF 500, Borchert+Moller) and cured in a convection oven (HTMA 6/220_3508 by Cabolite Gero). PET-meshes (with a 100 µm fiber diameter and pore size) were obtained by Eckert GmbH.

Electrostatic Flocking: Adhesive and hardener were thoroughly mixed in 1:1 wt.-ratio for ≈15 min. After 5 min of settling, the PET meshes were dip-coated with a thin adhesive layer and transferred to a paper towel.

The excessive adhesive was removed by squeegeeing with a glass rod. The adhesive-coated PET mesh was fixed on an aluminum foil as an electrode and placed below the flocking chamber. An electric field of 2.3 kV cm^{-1} was applied for 60 s. After a 10 s delay, the flock feed was switched on for 30 s. Finally, the PET mesh with the vertically deposited PA microfibers was placed onto a steel trail and transferred into a convection oven to crosslink the adhesive at 120 °C for 20 min. Afterward, the flock was stored for 24 h at RT to complete the adhesive curing. The samples were cleaned with pressured air to remove loose microfibers and subsequently washed with H_2O, ethanol, 2-propanol, and acetone and dried in a vacuum at 50 °C for 12 h.

Synthesis of N^1,N^3,N^5-tris[2-(Diisopropylamino)-ethyl]−1,3,5-Benzenetricarboxamide: N^1,N^3,N^5-tris[2-(diisopropylamino)-ethyl]−1,3,5-benzenetricarboxamide (BTA) was synthesized as described elsewhere.[30] Yield: 12.2°g (72%) of a white powder. ^{1}H-NMR (300 MHz, $CDCl_3$, δ): 1.06 (d, 36H), 2.71 (t, 6H), 3.07 (m, 6H), 3.45 (quartett, 6H), 7.23 (t(br), 3H), 8.41 (s, 3H) ppm. ^{13}C-NMR (75 MHz, CDCl3, δ): 20.9, 38.5, 42.8, 47.8, 127.8, 135.3, 165.2 ppm. MALDI-ToF MS m/z 589 $[M\bullet+H]^+$

Evaporation-Induced Self-Assembly of BTA from Solution: A clear solution containing 0.50 wt% of the BTA in 2-propanol was prepared at RT. 5 µL of this solution was dropped on a Si-wafer and the solvent was evaporated at ambient conditions.

Preparation of Supramolecular Spines on Top of PA Microfibers: The PA flock was immersed into a BTA solution of 0.50 wt% in 2-propanol for 30 s and placed for 10 s on a filtration paper to partially remove the BTA solution. The specimen was then placed in a petri dish, covered with aluminum foil and stored at 30 °C for complete solvent evaporation.

Characterization: ^{1}H-NMR (300 MHz) and ^{13}C-NMR (75 MHz) spectra were recorded on a Bruker Avance AC 300 spectrometer at room temperature. Matrix-assisted laser desorption/ionization time-of-flight mass spectroscopy (MALDI-ToF MS) measurements were performed using a Bruker AutoFlex Max mass spectrometer equipped with a Smartbeam II laser. The analyte was embedded in the matrix material trans-2-[3-(4-tert-butylphenyl)−2-methyl-2-propenylidene]malononitrile (DCTB) in the matrix:analyte mass ratio 10:1. Flock samples and water transport were investigated by a digital optical microscope (Zeiss, Smartzoom5) with a 4.2-megapixel sensor. The objective (Zeiss PlanApo D5x/0.3FWD 30 mm, 101x-1010x magnification) was illuminated with a coaxial brightfield and ring light. Scanning electron microscopy (SEM) was performed using an FEI Quanta FEG 250 (Thermo Fisher Scientific) equipped with a field emission gun. To minimize charging effects, the samples were sputtered (Cressington 208HR with planetary stage and QCM crystal) with platinum (2 nm) to create a conductive layer. SEM images were recorded in the low vacuum mode (water pressure of 60 Pa in the sample chamber) with an acceleration voltage of 3–5 kV using a large-field (gaseous secondary electron) detector (LFD) or with an acceleration voltage of 1–5 kV in the high vacuum mode using an Everhart–Thornley detector (EDT). The water condensation behavior and wettability of non-sputtered supramolecular spines and neat PA microfibers were investigated by the environmental scanning electron microscope (ESEM) FEI Quanta FEG 250 (Thermo Fisher Scientific) equipped with a Peltier cooling stage (ThermoFisher) and a gaseous secondary electron detector (GSED). ESEM images were recorded with an acceleration voltage of 10 kV. Measurements were carried out at a constant water pressure of 720 Pa and upon cooling the sample from 3.9to 1.9 °C (at a rate of 1 °C min^{-1}). Polarized Raman Spectroscopy was performed with a WITec Alpha RA+ imaging system, equipped with a UHTS 300 spectrometer and a back-illuminated Andor Newton 970 EMCCD camera for confocal Raman imaging. The measurements were conducted at an excitation wavelength of $\lambda = 532$ nm, using a laser power of 5 mW and an integration time of 1 s. All spectra were subjected to a cosmic ray removal routine and baseline correction.

Supporting Information

Supporting Information is available from the Wiley Online Library or from the author.

Acknowledgements

The authors thank Sandra Opel (Macromolecular Chemistry I, University of Bayreuth) for the support with the synthesis of the BTA. The authors acknowledge the support of the facility in the Keylab Electron and Optical Microscopy of the Bavarian Polymer Institute and in particular Dr. Ulrich Mansfeld for preliminary measurements and supporting discussions regarding the environmental-SEM (ESEM). The authors thank Lothar Benker (Macromolecular Chemistry II, University of Bayreuth) for conducting the RAMAN spectroscopy measurements. The authors also thank the Botanical Garden of the University of Bayreuth for providing cactus spines of the mammillaria neocoronaria.

Open Access funding enabled and organized by Project DEAL.

Conflict of Interest

The authors declare no conflict of interest.

Author Contributions

M.W. and F.B. contributed equally to this work. M.W. and F.B. conceived the idea and developed the concept. F.B. conducted electrostatic flocking on PET meshes and M.W. the self-assembly experiments. M.W. and F.B. performed the water transport experiments as well as all optical and electron microscopy studies. F.B. and M.W. analyzed all microscopic and spectroscopic data. All authors contributed to the discussion of the study and the interpretation of data. All authors were involved in preparing, writing and revising the manuscript.

Data Availability Statement

The data that support the findings of this study are available from the corresponding author upon reasonable request

Keywords

1,3,5-benzenetricarboxamides, hierarchical self-assembly, polymer flock, superhydrophilicity, supramolecular conical microstructures, water transport

Received: February 28, 2024
Revised: April 23, 2024

---

[1] G. M. Whitesides, B. Grzybowski, *Science* **2002**, 295.
[2] H.-W. Schmidt, F. Würthner, *Angew. Chem., Int. Ed.* **2020**, *59*, 8766.
[3] A. Aida, E. W. Meijer, I. Stupp, *Science* **2012**, *335*, 813.
[4] U. G. K. Wegst, H. Bai, E. Saiz, A. P. Tomsia, R. O. Ritchie, *Nat. Mater.* **2015**, *14*, 23.
[5] A. Gautieri, S. Vesentini, A. Redealli, M. J. Buehler, *Nano Lett.* **2011**, *11*, 757.
[6] J.-Y. Rho, L. Kuhn-Spearing, P. Zioupos, *Med Eng Phys* **1998**, *20*, 92.
[7] J. Ju, H. Bai, Y. Zheng, T. Zhao, R. Fang, L. Jiang, *Nat. Commun.* **2012**, *3*, 1247.
[8] F. T. Malik, R. M. Clement, D. T. Gethin, M. Kiernan, T. Coral, P. Griffiths, D. Beynon, A. R. Parker, *Philos. Trans. Royal Soc. A* **2016**, *374*.
[9] U. Schlegel, *Bradleya* **2009**, *27*, 129.
[10] D. Gurera, B. Bhushan, *Philos Trans A Math Phys Eng Sci* **2020**, *378*, 20190444.

[11] F. T. Malik, R. M. Clement, D. T. Gethin, D. Beysens, R. E. Cohen, W. Krawszik, A. R. Parker, *Bioinspir. Biomim.* **2015**, *10*, 036005.
[12] É. Lorenceau, D. Quéré, *J Fluid Mech* **2004**, *510*, 29.
[13] D. Zhan, Z. Guo, *Mater. Horiz.* **2023**, *10*, 4827.
[14] H. Lu, W. Shi, Y. Guo, W. Guan, C. Lei, G. Yu, *Adv. Mater.* **2022**, *34*, 2110079.
[15] S. Zhang, Y. Huang, Z. Chen, Y. Lai, *Small* **2017**, 13.
[16] F. Bai, J. Wu, G. Gong, L. Guo, *Adv. Sci.* **2015**, *2*, 1500047.
[17] H. Zhou, M. Zhang, C. Li, C. Gao, Y. Zheng, *Small* **2018**, *14*, e1801335.
[18] J. Ju, K. Xiao, X. Yao, H. Bai, L. Jiang, *Adv. Mater.* **2013**, *25*, 5937.
[19] Y. Liu, J. Liu, C. Chen, *Ind. Eng. Chem. Res.* **2023**, *62*, 10668.
[20] M. Cao, J. Ju, K. Li, S. Dou, K. Liu, L. Jiang, *Adv. Funct. Mater.* **2014**, *24*, 3235.
[21] S. Yi, J. Wang, Z. Chen, B. Liu, L. Ren, L. Liang, L. Jiang, *Adv. Mater. Technol.* **2019**, *4*, 1900727.
[22] X. Heng, M. Xiang, Z. Lu, C. Luo, *ACS Appl. Mater. Interfaces* **2014**, *6*, 8032.
[23] Y. Guo, Y.-Q. Luo, L. Liu, C. Ma, C. Liu, J. Wang, X. Gao, X. Yao, J. Ju, *J. Mater. Chem. A* **2023**, *11*, 12080.
[24] Y. Choi, K. Baek, H. So, *Sci. Rep.* **2023**, *13*, 10691.
[25] X. Li, Y. Yang, L. Liu, Y. Chen, M. Chu, H. Sun, W. Shan, Y. Chen, *Adv. Mater. Interfaces* **2020**, *7*, 1901752.
[26] D. Chen, J. Li, J. Zhao, J. Guo, S. Zhang, T. A. Sherazi, A. Ambreen, S. Li, *J. Colloid Interface Sci.* **2018**, *530*, 274.
[27] A. McCarthy, R. Shah, J. V. Johnson, D. Brown, J. Xie, *Appl. Phys. Rev.* **2021**, *8*, 41326.
[28] S. Cantekin, T. F. A. de Greef, A. R. A. Palmans, *Chem. Soc. Rev.* **2012**, *41*, 6125.
[29] D. Weiss, D. Skrybeck, H. Misslitz, D. Nardini, A. Kern, K. Kreger, H.-W. Schmidt, *ACS Appl. Mater. Interfaces* **2016**, *8*, 14885.
[30] A. Frank, M. Weber, C. Hils, U. Mansfeld, K. Kreger, H. Schmalz, H.-W. Schmidt, *Macromol. Rapid Commun.* **2022**, *43*, 2200052.
[31] C. Luo, *Langmuir* **2015**, *31*, 11809.
[32] D. Gurera, B. Bhushan, *Philos. Trans. Royal Soc. A* **2019**, *377*, 20180269.
[33] R. N. Wenzel, *Ind. Eng. Chem.* **1936**, *28*, 988.
[34] M. Brugnara, *Microsc. Anal.* **2007**, *21*, 17.
[35] H. Chen, T. Ran, Y. Gan, J. Zhou, Y. Zhang, L. Zhang, D. Zhang, L. Jiang, *Nat. Mater.* **2018**, *17*, 935.
[36] J. Wang, S. Yi, Z. Yang, Y. Chen, L. Jiang, C.-P. Wong, *ACS Appl. Mater. Interfaces* **2020**, *12*, 21080.
[37] A. Marmur, *Langmuir* **2003**, *19*, 8343.
[38] E. Bormashenko, *Adv. Colloid Interface Sci.* **2015**, *222*, 92.
[39] K. Wan, X. Gou, Z. Guo, *J Bionic Eng* **2021**, *18*, 501.
[40] A. B. D. Cassie, S. Baxter, *Trans. Faraday Soc.* **1944**, *40*, 546.
[41] J. Bico, U. Thiele, D. Quéré, *Colloids Surf. A.* **2002**, *206*, 41.
[42] S. Herminghaus, *Europhys. Lett.* **2000**, *52*, 165.